J Sol-Gel Sci Technol (2016) 79:295–302
DOI 10.1007/s10971-016-4052-x

ORIGINAL PAPER: FUNCTIONAL COATINGS, THIN FILMS AND MEMBRANES (INCLUDING DEPOSITION TECHNIQUES)

In situ growth of Ag nanoparticles in graphene–TiO_2 mesoporous films induced by hard X-ray

Luca Malfatti[1] · Davide Carboni[1] · Alessandra Pinna[1] · Barbara Lasio[1] · Benedetta Marmiroli[2] · Plinio Innocenzi[1]

Received: 4 March 2016 / Accepted: 13 April 2016 / Published online: 29 April 2016

Abstract The controlled growth of Ag nanoparticles into graphene–TiO_2 mesoporous films has been triggered by hard X-ray exposure provided by a synchrotron storage ring. The kinetic process has been studied by UV–visible spectroscopy as a function of the X-ray dose and compared to the nanoparticle growth induced in a bare mesoporous titania matrix. The graphene layers act as a preferential nucleation sites, allowing a faster nucleation of the nanoparticles. Moreover, the growth of larger nanoparticles is also promoted as a function of the exposure dose. The combined bottom-up and top-down approach to fabricate nanocomposites porous films embedding both graphene and plasmonic nanoparticles is expected to be a fundamental tool for the design of new analytical platforms based on the enhancement of the Raman signals.

Graphical Abstract

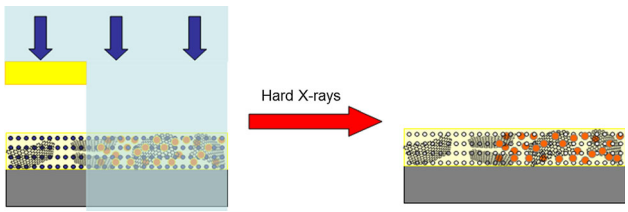

✉ Luca Malfatti
luca.malfatti@uniss.it

[1] Laboratorio di Scienza dei Materiali e Nanotecnologie, LMNT-D.A.D.U., CR-INSTM, Università di Sassari, Palazzo Pou Salit, Piazza Duomo 6, 07041 Alghero, Sassari, Italy

[2] Institute of Inorganic Chemistry, Graz University of Technology, Stremayrgasse 9/IV, 8010 Graz, Austria

Keywords Exfoliated graphene · Mesoporous films · Nanocomposites · Silver nanoparticles

1 Introduction

To be used in sensing applications, graphene-based nanocomposites require a highly interacting surface area available for the detection of specific molecules and analytes at low concentrations. Taking into account these requirements, we have recently prepared nanocomposite materials by embedding exfoliated graphene (EG) into mesoporous thin films [1]. These matrixes allow for an efficient incorporation of EG without affecting the pore organization during self-assembly. In addition, the synergy between host species and transition metal oxides, such as nanocrystalline TiO_2, enables the amplification of functional properties such as photocatalytic activity [2] or titania-induced graphene-mediated enhanced Raman scattering (Ti-GERS) [3]. Moreover, the use of a mesoporous scaffold enhances the interacting area of the nanocomposites providing an increased surface, i.e. the pore surface in the accessible matrix [4]. However, although Ti-GERS has shown a certain potential in the development of innovative analytical approaches, the low analytical enhancement factor (AEF) obtained by this approach is still the most critical drawback. The simultaneous use of the surface-enhanced Raman scattering (SERS) with the Ti-GERS would be an alternative route to achieve both the high enhancement factors, usually reached by the plasmonic amplification, and the selectivity provided by the TiO_2–graphene-mediated amplification. In a previous work, we have already explored a similar strategy by nucleating in situ gold nanoparticles at the interface of EG layers embedded into a mesoporous silica matrix [5]. The nanocomposite substrates allowed activating the graphene-

mediated surface-enhanced Raman scattering (G-SERS) where the enhancement of the Raman signal was cooperatively provided by graphene and plasmonic nanoparticles. Based on our previous experiments, therefore, we expect that the nucleation of noble metal nanoparticles in a mesoporous matrix made by titania and EG layers would provide an even higher enhancement using the amplification of titania–graphene films and plasmonic particles.

Mesoporous oxides have shown to be an ideal matrix for growing a large variety of nanoparticles (NPs), ranging from transition metal and metal oxide NPs [6, 7], quantum dots [8, 9] and particles bearing plasmonic properties [10–14]. In particular, we have recently shown that deep X-ray lithography can be efficiently used as a top-down lithographic method for the nucleation of ceria nanoparticles in the pores of a pre-formed titania matrix [15]. After deposition and processing, the samples have been at first impregnated with a suitable solution containing the NPs precursor and a coordinating agent (such as ionic or non-ionic surfactants). Then, they have been directly exposed to hard X-rays provided by a synchrotron storage ring. The high penetration depth of the X-ray beam allows for an efficient NPs growth within the whole film thickness, while the interaction with the OH groups on the film surface triggers the production of a large amount of radical species which are responsible for the NPs formation [16, 17].

In this work, we have studied how the X-rays-induced growth of Ag NPs in mesoporous films is affected by the addition of EG into the matrix. Both mesopore surface and graphene layers, in fact, play as nucleation sites for nanoparticles; however, to the best of our knowledge, there are no studies focused on the NPs growth within nanocomposite and porous matrix.

2 Experimental

2.1 Chemicals

N-Vinyl-2-pyrrolidone (NVP, Sigma-Aldrich), graphite (Sigma-Aldrich), titanium tetrachloride ($TiCl_4$, Aldrich), triblock copolymer Pluronic F127 ($OH(CH_2–CH_2O)_{106}–(CHCH_3CH_2O)_{70}(CH_2CH_2-O)_{106}$, Sigma), silver nitrate ($AgNO_3$, Aldrich), ethanol (EtOH, Fluka) and distilled water were used as received without further purification. *p*-Type/boron-doped, (100)-oriented, 381-μm-thick silicon wafers (Si-Mat) and 1.2-mm-thick silica slides (UV grade) were used as substrates.

2.2 Graphene dispersion

A graphene batch solution was prepared by dispersing 5 wt% graphite flakes in NVP, placing it into a tubular plastic reactor (inner diameter 15 mm) and ultrasonicating it for 24 h at 25 °C (Ultrasound bath EMMEGI, 0.55 kW). The dispersion was then centrifuged for 30 min at 4000 rpm to allow recovering the grey-to-black liquid phase containing graphene. Gravimetric filtration through polyvinylidene fluoride (PVDF) filters (pore size 220 μm) allowed obtaining a concentration of the graphene dispersion equal to 2.27 mg mL^{-1}.

2.3 Sol preparation

The titania precursor sol was prepared using $TiCl_4$, EtOH, H_2O and Pluronic F127, with the following molar ratios: $TiCl_4$:EtOH:F127:H_2O = 1:40:0.005:10. The precursor sol was obtained by addition of $TiCl_4$ into a mixture of EtOH and surfactant Pluronic F127 after 5 min of stirring; water was then added dropwise at the precursor sol. As a final step, 25 μl of exfoliated graphene (EG) dispersion was added to 2 mL of titania precursor sol, and the mixture was left under stirring for other 10 min.

The titania sol was then deposited by spin coating onto silicon and silica substrates using a rotation speed of 3000 rpm for 40 s followed by 300 rpm for 30 s. The substrates were previously cleaned with acetone and ethanol. After deposition, the films were fired in an oven at 350 °C for 2 h.

2.4 Silver nitrate impregnation

A silver nitrate stock solution was prepared by adding 0.25 g of $AgNO_3$ in 30 mL of EtOH. Titania and EG–titania thin films were impregnated in 10 mL of an $AgNO_3$ solution by fully immersing them for 15 min in a plastic Petri dish, after which the impregnated films were drained off the liquid residues, washed by immersing them in fresh EtOH and dried with compressed nitrogen.

2.5 Hard X-ray exposure

The impregnated films were exposed soon after to hard X-ray radiations using the deep X-ray lithography (DXRL) beamline at the Elettra synchrotron facility (Trieste, Italy). The storage ring worked at 2.4 GeV. Each sample was mounted on top of a water-cooled stainless-steel plate (scanner), which was continuously moving in front of the beam to allow for a homogeneous exposure of areas larger than the beam size; the scanner rate was set to 20 mm s^{-1}. At the exposure plane (position of the sample), the beam size was 115.5 mm × 10.6 mm. Two films (with and without EG, respectively) were exposed in pair to increasing doses starting from 41 J cm^{-2} and increasing gradually the dose stepwise by 41 J cm^{-2} per exposure, until reach the overall dose of 204 J cm^{-2} (82, 122, 163,

204 J cm^{-2}). The same samples were then re-exposed to a dose of 122 and 326 J cm^{-2}, to reach a total dose of 326 and 652 J cm^{-2} respectively. A final exposure to a dose equal to 848 J cm^{-2} brought to an overall dose of 1500 J cm^{-2}. The Ag NPs growth was evaluated after each exposure on both films, with and without EG, by means of UV–Vis spectroscopy using the corresponding not exposed, and not impregnated, film as a background reference.

2.6 Materials characterization

A Bruker Senterra confocal Raman microscope working with a laser excitation wavelength of 532 nm at 12.5 mW of nominal power was used for optical microscopy (100 × magnification) and Raman spectroscopy analysis; the spectra were recorded by averaging 30 acquisitions of 2 s.

Fourier transform infrared (FTIR) measurements were obtained by using an "Alpha" spectrophotometer, from Bruker Optics, equipped with a DTGS detector and a KBr beam splitter. The spectra were recorded in the 400–4000 cm^{-1} range with a resolution of 4 cm^{-1} using a silicon wafer as the background reference. The baseline was corrected using a concave rubber-band method (OPUS 6.5 software) using 64 baseline points and one iteration.

Transmission electron microscopy (TEM) images were obtained by using two different microscopes working with field emission electron guns: a JEOL JEM 1011 operating at 100 kV, equipped with a spherical aberration corrector, and a FEI TECNAI 200 operating at 200 kV. Sample preparation was done by scratching the films, dispersing the fragments in ethanol by ultrasonication and then dropping them onto a carbon-coated copper grid and drying them for observations.

The film thickness and residual porosity were estimated by a α-SE Woollam spectroscopic ellipsometry using a Bruggeman effective medium approximation fitting model with two components: void and Cauchy film. The refractive index parameters for the Cauchy film model were measured on reference samples treated at 350 °C, made by dense titania and not containing the templating agent. Plots of Ψ and Δ as a function of incident wavelength from 400 to 900 nm were simulated using "CompleteEASE v. 4.2" program from Woollam. The results of the fits were evaluated on the basis of the mean squared error (MSE), which was maintained below 14.

Optical properties of films, in the range 200–800 nm, were measured by using a UV–Vis spectrophotometer Cary 60, from Agilent Technologies, equipped with a sample holder suitable for films. Mesoporous titania and titania–EG deposited on silica were used as background references for TiO_2/Ag and graphene–TiO_2/Ag films, respectively.

3 Results and discussion

To study the effect of hard X-rays on the growth of Ag NPs, we have used a bare mesoporous TiO_2 film and a similar film containing exfoliated graphene (EG). The latter has been prepared through a one-pot approach, making use of an optimized amount of a graphene colloidal suspension in *N*-Vinyl-2-pyrrolidone (NVP) added to the sol used for the deposition (25 µl in 2 mL of the titania sol). This method has already proved to allow incorporating a sufficient amount of EG into mesoporous films, without affecting the pore organization during the evaporation-induced self-assembly. Moreover, the hydrophilicity of the NVP suspension enables a homogeneous dispersion of the graphene layers within the inorganic matrix.

The annealing temperature of the samples (350 °C) has been chosen in order to keep the mesopore organization, achieved by self-assembly, and facilitate the complete removal of the templating agent. Higher temperature would have been caused a higher crystallinity of the inorganic matrix with a partial collapse of the mesopores, inducing a strong change in the pore size and therefore affecting the Ag NPs nucleation and growth. Figure 1a, b shows the FTIR spectra of the two different matrixes before and after thermal treatment, in the range of 4000–1000 cm^{-1}. The clearest difference between the spectra of the two as-deposited films (black lines) is given by the two bands peaked at 1670 cm^{-1}. This has been attributed to the most intense absorption band of NVP, which is the C=C stretching of the vinyl groups [18]. Another difference is the intensity of the band peaked at 1113 cm^{-1} which is mainly due to the C–O–C stretching of the block copolymer (Pluronic F127) used as a templating agent. However, in the case of the graphene–TiO_2 sample, a secondary contribution to this band can be due to the presence of C–OH which is formed as a consequence of the partial oxidation of the NVP monomers during the microwave treatment used for the graphene exfoliation. After thermal treatment, both pure TiO_2 and nanocomposite graphene–TiO_2 show similar FTIR spectra (blue line of Fig. 1a and red line of Fig. 1b). The strong reduction of the broadband between 3750 and 2750 cm^{-1} has been attributed to the reduction of adsorbed water and the increase in the polycondensation of the titania network. Interestingly, the addition of the EG in NVP does not seem to change the amount of adsorbed water in the mesoporous films, indicating that the hydrophilicity of the sample is not affected by the EG addition. The thermal degradation of block copolymer and NVP has been confirmed by the decrease in the three different bands between 3010 and 2800 cm^{-1} attributed to –CH_3 asymmetric, –CH_2 asymmetric and –CH_3 symmetric stretching modes, respectively. A similar decrease is also

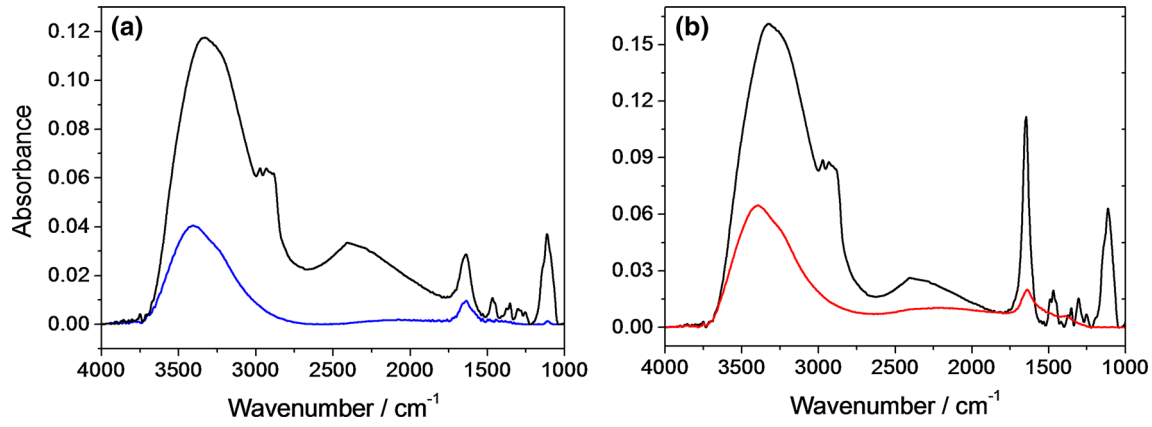

Fig. 1 FTIR spectra, in the range of 4000–1000 cm^{-1}, of titania mesoporous films without exfoliated graphene (**a**) and with exfoliated graphene (**b**) as-deposited (*black lines*) and after being treated 2 h at 350 °C (*blue* and *red lines*) (Color figure online)

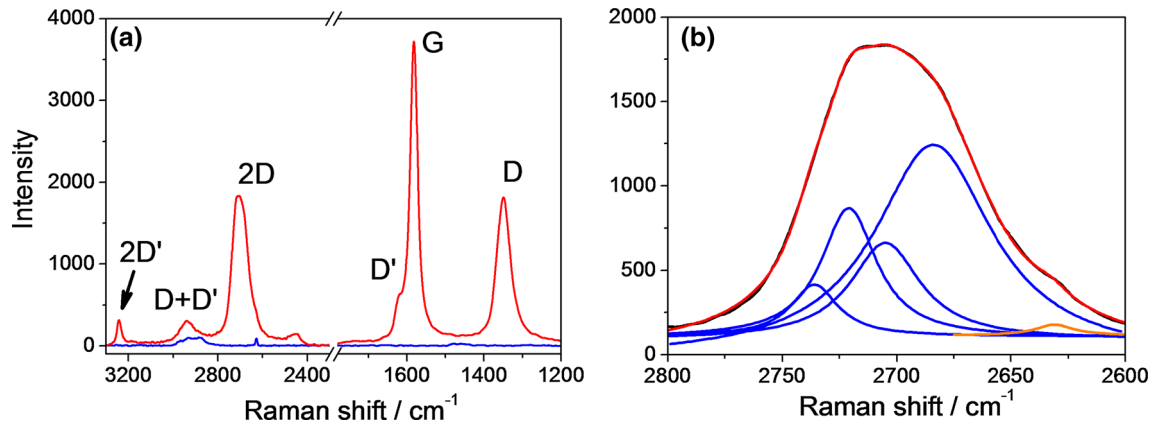

Fig. 2 **a** Raman spectra in the range of 3300–1200 cm^{-1} of titania mesoporous films with (*red line*) and without exfoliated graphene (*blue line*) after being treated 2 h at 350 °C; **b** Raman spectra of titania mesoporous films in the range of 2800–2600 cm^{-1}, with exfoliated graphene, after the thermal treatment at 350 °C. The *black curve* shows the acquired Raman spectrum, while the *red line* describes the fitting obtained by combining the Lorentzian curves (*blue curves*). The orange line centred at 2627 cm^{-1} is the fitted band of the silicon signal (Color figure online)

observed in the band peaked at 1113 cm^{-1} where intense absorption bands of the two organic compounds are located.

Raman spectroscopy has been then used to characterize the EG into the titania matrix after thermal annealing (Fig. 2a, b). Figure 2a shows a typical spectrum of the graphene–TiO_2 nanocomposite (red line) with respect to the pure titania film (blue line) in the range of 3300–1200 cm^{-1}. All the bands can be easily attributed to the peculiar vibrations of the graphene structure. In particular, the ratio R between the relative intensities of the D and G bands can be used as a tool to estimate the lack of order in the graphene layer. The *R* value, in fact, is ≥1 if the graphene layers contain many oxidized C atoms, such as when it is in form of graphene oxide. On the contrary, the *R* value is almost zero in pure graphite where the D band is barely detectable. The Raman spectrum of exfoliated graphene is an intermediate case as it clearly shows the D band, but with a lower intensity with respect to the G band. This can be explained, considering that the number of defects at the edges of the EG layers is higher compared to pure graphite; however, the mechanical exfoliation does not require a complete oxidation, leading to a less defective structure if compared to that of graphene oxide [19, 20].

Figure 2b shows the results of the 2D band fit with a set of Laurentian curves. This analysis is of particular importance as it allows identifying whether the graphene is in form of monolayer or rather in form of platelets (few-layer graphene). The number of Laurentian curves that allow fitting the 2D band, in fact, can be associated with the number of graphene sheets in the aggregates [21]. As shown in the figure, the best results have been obtained by using 4 fitting curves (an additional curve has been used to

Table 1 Spectroscopic ellipsometry analysis of titania mesoporous films, with and without exfoliated graphene, as-deposited and after a thermal treatment of 2 h at 350 °C

Sample	Thickness (nm)	Refractive index
TiO_2 as-deposited	328 ± 14	1.69
TiO_2 350 °C	129 ± 5	1.77
TiO_2–graphene as-deposited	341 ± 14	1.70
TiO_2–graphene 350 °C	143 ± 3	1.78

fit the absorption of the silicon substrate), indicating the presence of well-defined two-layer graphene in the TiO_2 nanocomposite films.

Spectroscopic ellipsometry has been also used to characterize the films before NPs growth (Table 1). Both the bare TiO_2 and the graphene–TiO_2 samples have a similar thickness, which is in the range of 330–340 nm after deposition and 130–140 nm after thermal annealing. The nanocomposite films, however, are slightly thicker ($\approx$10 nm) and with a higher refractive index. These changes have been attributed to the addition of the EG colloidal solution to the initial sol; an increase in viscosity due to the NVP addition, in fact, can be responsible of the higher thickness, while the presence of EG affects the refractive index.

The nucleation of Ag NPs in the mesoporous matrix has been induced by hard X-ray exposure using a synchrotron storage ring facility. This technique enables a fast production of radicals within the porous matrix, and the radical species can be effectively used to chemically modify the film composition. The high penetration depth of X-ray radiation allows for a homogeneous effect in the matrix, even for several-micron thick films [22]. The protocol used for Ag NPs growth is resumed in the schematic of Fig. 3. After deposition, the films have been thermally treated to remove the templating agent and open the mesopores (Fig. 3a). Then, the pores have been filled by immersing the samples into an ethanol solution of silver nitrate (Fig. 3b). After draining and washing with fresh ethanol, the films have been dried with compressed nitrogen and exposed to increasing X-ray doses. The NPs growth has been monitored as a function of the dose (Fig. 3c). The range of X-ray doses, i.e. the energy impinging on the sample surface, has been carefully chosen on the basis of previous experiments, to monitor both nucleation and growth stages. As extensively shown in previous works, the exposure to hard X-ray also allows patterning the surface with a high spatial resolution, thanks to the short wavelength of the X-ray radiation (Fig. 3d) [10, 11].

Figure 4 shows the effects of X-ray exposure on the UV–Vis absorption of the samples. Higher doses cause a higher absorption in the 350–670 nm range that is attributed to the plasmon resonance of small Ag NPs. Interestingly, the kinetics of the nanoparticles growth appears to be different when the Ag NPs are nucleated in bare TiO_2 with respect to graphene–TiO_2 matrix. The maximum of the plasmonic band, in particular, is constant at $\approx$480 nm in the first case, while gradually shifts from $\approx$479 to around 484 nm in the second one. The red shift of the surface plasmon resonance with increasing exposure doses has been attributed to the growth of larger nanoparticles with respect to those nucleated in the bare mesoporous TiO_2

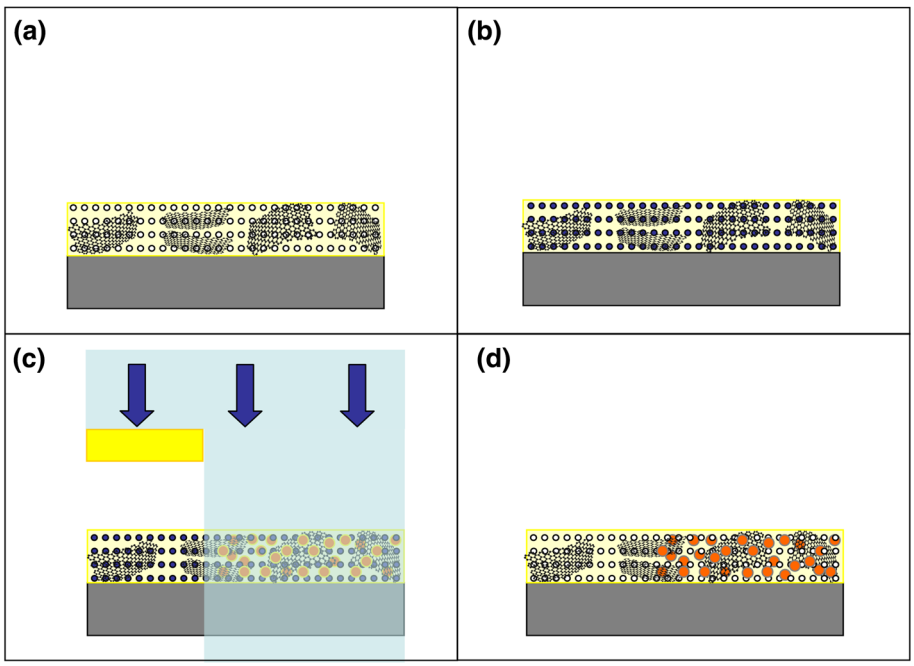

Fig. 3 Scheme describing the impregnation and exposure of mesoporous titania films to hard X-rays. **a** Preparation of films; **b** impregnation of films with a silver nitrate ethanol solution; **c** exposure to hard X-ray through a lithographic mask induces particles nucleation and growth; **d** film development.

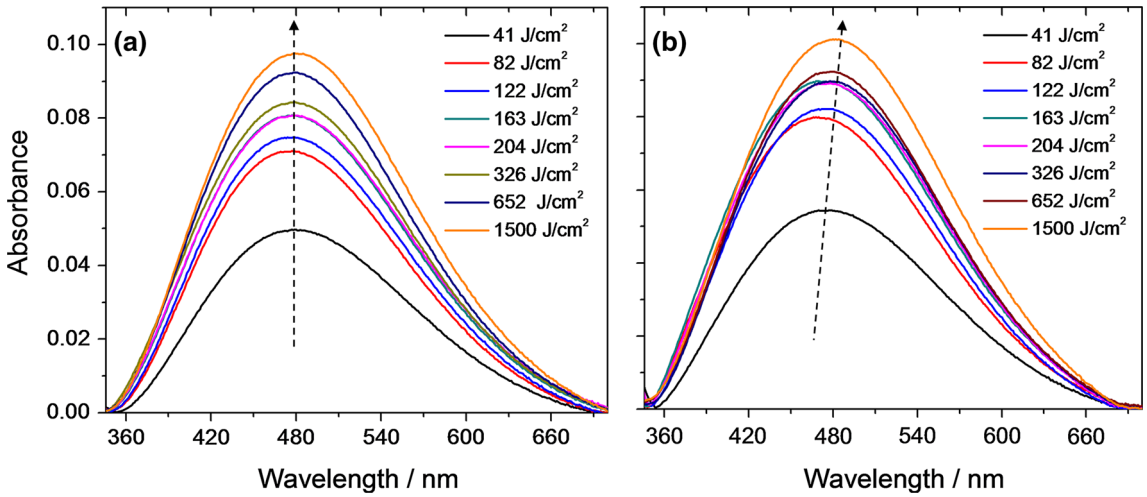

Fig. 4 UV–Vis spectra of titania mesoporous films, in the range of 350–700 nm, describing the increase in the Ag plasmon resonance as a function of the hard X-ray doses for film not containing (**a**) and containing exfoliated graphene (**b**)

films. According to the generalized Mie theory, in fact, it has been shown that the maximum of the surface plasmon resonance of Ag NPs into mesopores of TiO_2 can be modulated from 385 to 490 nm by varying the NPs size from 3 to 4 nm. This estimation has been obtained by modelling the NPs in the pores as a core–shell nanostructure where the metal core and the pore are supposed to form a concentric spherical heterosystem [23]. It is also important to stress that the NPs size is still smaller than that of the mesopores, which is in the range of 5–6 nm, as previously observed [2]. The higher NPs size in the graphene–TiO_2 can be attributed to the presence of the two-layer graphene at the pore surface. In particular, it has been previously shown that reduced graphene and graphene oxide structures are not only good substrates for the dispersion of metal NPs, but they also can work as preferential sites for the photo-reduction of metal ions because of the defects which are present in their structure [24, 25]. These findings also confirm, although indirectly, that some of the graphene sheets are available on the mesopore surface and are not completely embedded into the pore walls.

TEM investigation has been performed on some film fragments to analyse the nanocomposite structures after NPs nucleation at the highest X-ray dose (Fig. 5). The pore structure is well organized and shows a periodicity, which is compatible with a body-centred cubic arrangement ($Im\bar{3}m$), although some regions appear formed by channels. This feature has been already explained as the merging of different pore planes due to TEM focusing effect (Fig. 5a, b) [26]. The pore size and wall thickness have been measured from plot profile of selected TEM images, resulting in 4.4 ± 0.8 and 5.0 ± 0.6 nm, respectively. A careful analysis of Fig. 5b also reveals the presence of small spherical regions with a higher contrast with respect to the inorganic host matrix. Characterization at higher magnification has allowed confirming that the darker round spots are due to crystalline phases compatible with the presence of Ag NPs (inset of Fig. 5b). A comparison between the bright- and dark-field TEM images of the same film fragment has allowed evaluating the NPs loading (Fig. 5c, d). In agreement with the presence of crystalline Ag NPs, the dark spots in the bright field appear as bright spots in dark field. This result, however, does not exclude a contribution coming from small titania crystallites, which can be present within the pore walls. As expected by the confined nucleation and growth, the NPs size is similar to that of the mesopores (3.6 ± 1.5 nm); however, it has not been possible to achieve a clear difference between the sizes of the NPs nucleated in the TiO_2 matrix with respect to those in the graphene–TiO_2 film.

The maxima of UV–Vis absorbance were then plotted as a function of the exposure dose in order to analyse the kinetic profile of the NPs growth (Fig. 6). In fact, considering that the film thickness of the FWHM of the plasmon resonance is quite similar in the TiO_2 and graphene–TiO_2 systems, an increase in the film absorbance at fixed position can be directly correlated with the NPs loading in the pores. Interestingly, the nanocomposite matrix shows a higher absorption even at the lowest X-ray dose, indicating that the NPs nucleation is favoured in the presence of EG. This assumption is further confirmed at intermediate doses (from 82 up to 326 J cm^{-2}) where the two experimental curves show a hyperbolic increase with a higher slope for the graphene–TiO_2 nanocomposites. Finally, the NPs loading seems to reach an asymptotic trend in the TiO_2 system, while the graphene–TiO_2 matrix shows a further increase in the plasmon resonance intensity even at the highest X-ray dose. To summarize, the trend in NPs

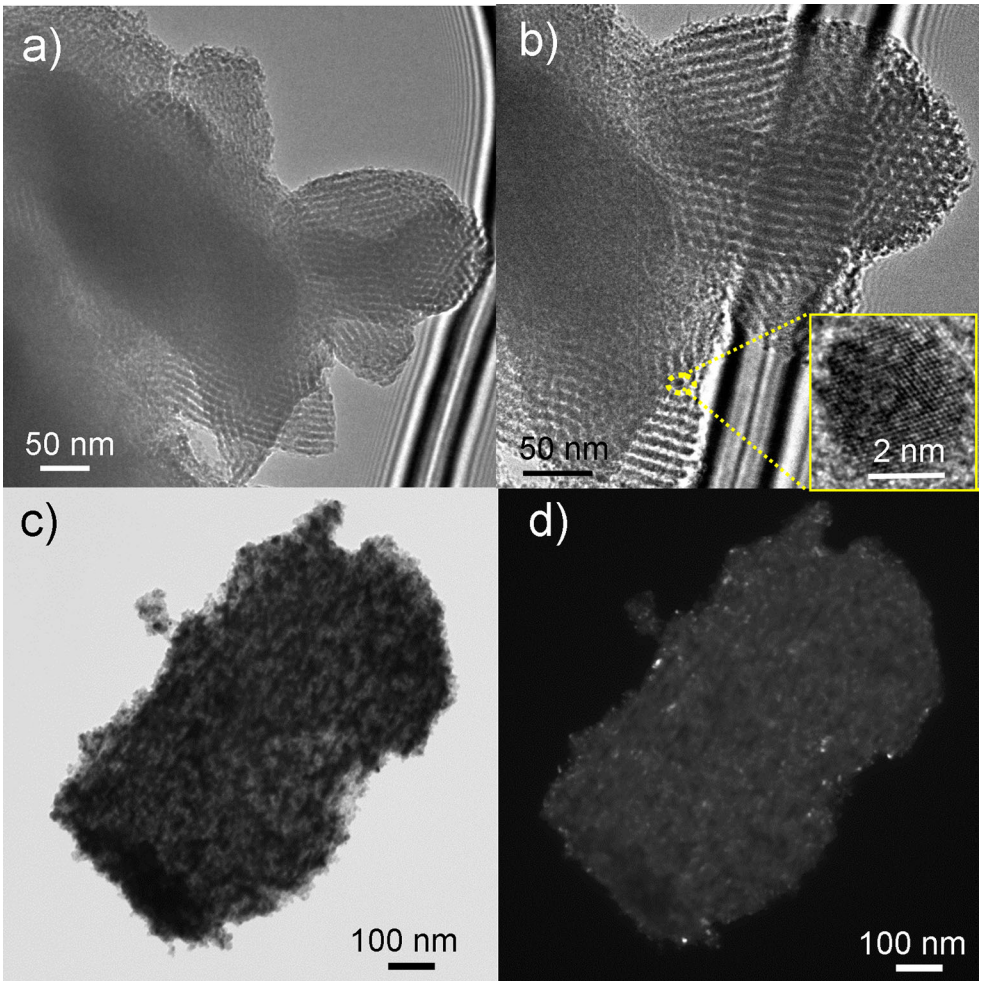

Fig. 5 **a**, **b** Bright-field TEM images of titania mesoporous films embedding exfoliated graphene (not visible) and crystalline Ag NPs (*inset* of **b**). **c**, **d** Bright and corresponding dark field of a titania mesoporous films embedding exfoliated graphene and silver nanoparticles. The *white spots* of **d** are attributed to crystalline Ag NPs

nucleation and growth shows that the EG is a preferential nucleation site with respect to the bare mesopore surface. This is confirmed by comparing the kinetic profile of the two systems at intermediate doses, suggesting that the EG is accountable for a higher nucleation rate of the nanoparticles within the matrix.

4 Conclusions

The nucleation and growth of Ag NPs in a graphene–TiO_2 mesoporous film have been studied as a function of the exposure to hard X-rays. As suggested by a comparative analysis of the UV–Vis spectra, the presence of exfoliated graphene in the mesoporous matrix is accountable for a larger growth with respect to a bare TiO_2 film. Moreover, the NPs loading is higher in the case of the graphene-doped matrix, suggesting that also the nucleation step of NPs is

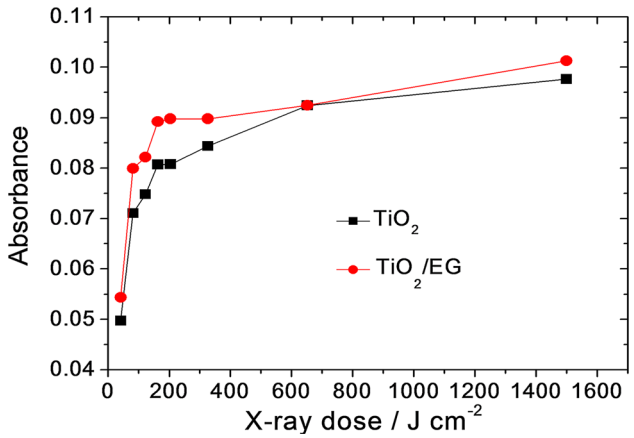

Fig. 6 Kinetic plots of UV–Vis absorption maxima of Ag plasmon resonance as a function of the hard X-ray doses, for titania mesoporous films with (*red dots*) and without (*black squares*) exfoliated graphene. The *lines* are guides for eyes (Color figure online)

favoured. The synthesis of controlled porous nanocomposite made by mesoporous titania, exfoliated graphene and Ag NPs is expected to open new possibilities in the design of new sensing substrates based on the enhanced Raman scattering.

Acknowledgments The authors acknowledge the CERIC-ERIC consortium for the access to experimental facilities and financial support. Alberto Mariani is gratefully acknowledged for providing the EG colloidal suspensions. Maria F. Casula is also acknowledged for TEM characterization.

References

1. Innocenzi P, Malfatti L, Carboni D (2015) Nanoscale 7:12759
2. Malfatti L, Falcaro P, Pinna A, Lasio B, Casula MF, Loche D, Falqui A, Marmiroli B, Amenitsch H, Sanna R, Mariani A, Innocenzi P (2014) ACS Appl Mater Interfaces 6:795
3. Carboni D, Lasio L, Loche D, Casula MF, Mariani A, Malfatti L, Innocenzi P (2015) J Phys Chem Lett 6:3149
4. Innocenzi P, Malfatti L (2013) Chem Soc Rev 42:4198
5. Carboni D, Lasio B, Alzari V, Mariani A, Loche D, Casula M F, Malfatti L, Innocenzi P (2014) Phys Chem Chem Phys 16:25809
6. Costacurta S, Malfatti L, Innocenzi P, Amenitsch H, Masili A, Corrias A, Casula MF (2008) Micropor Mesopor Mater 115:338
7. Hess DM, Naik RR, Rinaldi C, Tomczak MM, Watkins JJ (2009) Chem Mater 21:2125
8. Buso D, Falcaro P, Costacurta S, Guglielmi M, Martucci A, Innocenzi P, Malfatti L, Bello V, Mattei G, Sada C, Amenitsch H, Gerdova I, Haché A (2005) Chem Mater 17:4965
9. Besson S, Gacoin T, Ricolleau C, Jacquiod C, Boilot J-P (2002) Nano Lett 2:409
10. Malfatti L, Marongiu D, Costacurta S, Falcaro P, Amenitsch H, Marmiroli B, Grenci G, Casula MF, Innocenzi P (2010) Chem Mater 22:2132
11. Malfatti L, Falcaro P, Marmiroli B, Amenitsch H, Piccinini M, Falqui A, Innocenzi P (2011) Nanoscale 3:3760
12. Fuertes MC, Marchena M, Marchi MC, Wolosiuk A, Soler-Illia GJAA (2009) Small 5:272
13. Martínez ED, Bellino MG, Soler-Illia GJAA (2009) ACS Appl Mater Interfaces 1:746
14. Innocenzi P, Malfatti L, Marmiroli B, Falcaro P (2014) J Sol-Gel Sci Technol 70:236
15. Pinna A, Lasio B, Piccinini M, Marmiroli B, Amenitsch H, Falcaro P, Tokudome Y, Malfatti L, Innocenzi P (2013) ACS Appl Mater Interfaces 5:3168
16. Innocenzi P, Malfatti L, Falcaro P (2012) Soft Matter 8:3722
17. Falcaro P, Costacurta S, Malfatti L, Takahashi M, Kidchob T, Casula MF, Piccinini M, Marcelli A, Marmiroli B, Amenitsch H, Schiavuta P, Innocenzi P (2008) 20:1864
18. Medda SK, Kundu D, De G (2003) J Non-Cryst Solids 318:149
19. Green AA, Hersam MC (2010) J Phys Chem Lett 1:544
20. Innocenzi P, Malfatti L, Lasio B, Pinna A, Loche D, Casula MF, Alzari V, Mariani A (2014) N J Chem 38:3777
21. Malard LM, Pimenta MA, Dresselhaus G, Dresselhaus MS (2009) Phys Rep 473:51
22. Falcaro P, Costacurta S, Malfatti L, Buso D, Patelli A, Schiavuta P, Piccinini M, Grenci G, Marmiroli B, Amenitsch H, Innocenzi P (2011) ACS Appl Mater Interfaces 3:245
23. Bois L, Chassagneux F, Battie Y, Bessueille F, Mollet L, Parola S, Destouches N, Toulhoat N, Moncoffre N (2010) Langmuir 26:1199
24. Gotoh K, Kinumoto T, Fujii E, Yamamoto A, Hashimoto H, Ohkubo T, Itadani A, Kuroda Y, Ishida H (2011) Carbon 49:1118
25. Moon G, Kim H, Shinc Y, Choi W (2012) RSC Adv 2:2205
26. Crepaldi EL, Soler-Illia GJAA, Grosso D, Cagnol F, Ribot F, Sanchez C (2003) J Am Chem Soc 125:9776